Xenon and iodine behaviour in magmas

C. Leroy, H. Bureau, C. Sanloup, C. Raepsaet, K. Glazirin, P. Munsch, M. Harmand, G. Prouteau, H. Khodja

Xenon and iodine behaviour in magmas

C. Leroy[1], H. Bureau[*1], C. Sanloup†[2], C. Raepsaet[3], K. Glazirin[4], P. Munsch[5], M. Harmand[1], G. Prouteau[6], and H. Khodja[3]

[1] *Institut de Minéralogie, de Physique des Matériaux et de Cosmochimie (IMPMC), Sorbonne Université, CNRS UMR 7590, Muséum National d'Histoire Naturelle, 75005 Paris, France*

[2] *Institut des Sciences de la Terre de Paris,* Sorbonne Université*, CNRS, 4 place Jussieu, 75252 Paris Cedex 05, France*

[3] *LEEL, NIMBE, CEA, CNRS, Université Paris-Saclay, CEA Saclay, 91191 Gif-sur-Yvette Cedex, France*

[4]*DESY Photon Science, Notkestr. 85, 22607 Hamburg, Germany*

[5]*Institut de recherche sur les céramiques, IRCER – UMR CNRS 7315, 12, rue Atlantis, 87068 Limoges, France*

[6] *ISTO CNRS/INSU, BRGM, UMR 7327, Université d'Orléans,1A Rue de la Férollerie, 45071 Orléans, France*

Revised for *Earth and Planetary Sciences Letters*

*Corresponding author. *E-mail address*: helene.bureau@upmc.fr;

† Now at affiliation 1.

Abstract

Iodine (I) and xenon (Xe) are two key elements that trace Earth's differentiation (e.g. atmosphere formation) and dynamics (e.g. volcanism and recycling at subduction zones). Iodine and Xe abundances are linked through the decay of the extinct ^{129}I that produced ^{129}Xe, which is today depleted in the Earth's atmosphere compared to the composition of the solar system (i.e. chondrites). Iodine and Xe cycles and storage in the deep Earth are almost unknown, which is in large part due to the fact that their behaviour in magmas and fluids, key agents of mass transfer through planetary enveloppes, are poorly known. Here, the solubility of Xe and I in melts is measured under high pressure (*P*) and temperature (*T*) conditions using large volume presses, and Xe and I behaviour in melts and fluids is monitored in situ under high *P-T* conditions using resistive heating diamond anvil cells combined with synchrotron x-ray fluorescence (XRF) and Raman spectroscopy. Xenon, I and H (H_2O) contents were measured in quenched glasses by particle x-ray Emission (PIXE) and Elastic Recoil Detection Analysis (ERDA). Solubility, speciation and degassing processes are investigated for two different compositions: haplogranitic melt (HPG analogue for crustal melts) and basaltic melts (MORB and IAB). Experimentally measured solubilities for both elements are much higher than their natural abundances in terrestrial magmas. Xenon solubility at 3.5 GPa reaches 4.00 wt.% in HPG and 0.40 wt.% in basalts. Iodine solubility is 0.46 wt.% at 0.4 GPa on average in HPG, and reaches 1.42 wt.% in basalts at 2 GPa. The *in situ* Raman spectroscopic study shows that I forms I-I bonds in hydrous high P fluids/melts unlike Xe that was previously shown to oxidize in high P melts. The XRF monitoring of I and Xe partitioning

between aqueous fluids and silicate melts during decompression (i.e. water degassing) shows that Xe degassing is strongly *P-T* dependent and can be retained in the melt at deep crust conditions,, while I is totally washed out from the silicate melt by the aqueous phase. Xenon and I degassing processes are based on different mechanisms, which implies that the atmospheric isotopic signature of Xe cannot be inherited from a process involving volcanic water degassing. Instead, ^{129}Xe depletion may originate from a separation of both elements at depth, by deep fluids, a proposition that agrees with a deep storage of Xe in minerals.

Keywords iodine, xenon, silicate melt, solubility, speciation, volcanic degassing

1. Introduction

Iodine (I) and xenon (Xe) are highly volatile elements, differing only by one proton, but due to their difference in electron configuration, I is a very reactive halogen element while Xe is a noble gas. They share a very low abundance compared to chondrites in the Bulk Silicate Earth (BSE) and low temperatures of condensation (see Marty, 2012). Both I and Xe are potentially "missing" in the BSE compared to solar abundances. Iodine and Xe elements are neighbours in the periodic table, and are linked by the radioactive decay of the today extinct ^{129}I to ^{129}Xe (half life 16.1 million years).

Yet unsolved issues are: (1) why is the Earth's atmosphere depleted in elemental Xe and ^{129}Xe? (2) how are I and Xe recycled back to the mantle at subduction zones? (3) whether or not I and Xe are stored in the deep Earth, and if so, by which processes and to what extent?

Iodine is the heaviest stable halogen element, having the largest ionic radius, and for this reason it is much less frequently incorporated in minerals than chlorine (Cl) and bromine (Br) (McDonough and Sun, 1995), whereas they shares many other characteristics. Iodine is mostly found at the ppb level in magmatic rocks and volcanic glasses (Muramatsu and Wedepohl, 1998; Schilling et al., 1980; Déruelle et al., 1992; Kendrick et al., 2012). It is more concentrated in sediments than in any other geologic materials (Muramatsu and Wedepohl, 1998). Being hydrophilic and biophilic, it is enriched in marine organic matter and associated fluids (Fehn 2012). ^{129}I is used to trace crustal

and volcanic fluids in subduction contexts (Fehn, 2012), where serpentinites are efficient traps for subducted I (John et al., 2011; Kendrick et al., 2012). Experimental studies have demonstrated that heavy halogens Br and I may significantly degas from hydrous silicic magmas (Bureau et al., 2000; 2010; 2016). The uncertainty on I outgassing fluxes is due to the lack of constraints on: (1) the real I content of magmas; (2) the storage capacity of magmas with respect to I, and more specifically I solubility in melts relevant for subduction-related volcanism; (3) the real abundance of I in the bulk silicate Earth, (4) how much of subducted I is deeply recycled. Mass balance calculations based on the I content of MORBs (Mid Ocean Ridge Basalts) have been used to predict the total amount of I in the bulk silicate Earth (McDonough and Sun, 1995), resulting in a strong depletion of the BSE compared to solar compositions (i.e. CI chondrites). Two scenarios are proposed: (1) I loss by a strong degassing event of the magma ocean during the Hadean eon (Bureau et al., 2016); (2) I storage in the core (Armytage et al., 2013) or in a hidden deep mantle reservoir(s). Alternatively, there could be no I depletion as indicated by new measurements of halogen contents in chondrites (Clay et al. 2018).

As most noble gases, Xe is a tracer of Earth's dynamics. Xenon isotopes are important markers of planetary processes, and the I-Pu-Xe system is used to date the formation of the atmosphere (Ozima and Podosek, 1999, Pepin 2006, Avice and Marty 2014). About 90% of Earth's primordial Xe is missing from the atmosphere of the Earth (Anders and Owen 1977, Ozima and Podosek, 1999), this is the "missing Xe" issue. Xenon is depleted by one order of magnitude relative to other volatile elements (water, carbon, neon, argon and krypton) when normalized to the chondritic composition, and atmospheric Xe is enriched in heavy isotopes by 3–4% amu^{-1} (unified atomic mass unit) relative to chondritic and solar compositions, this is the "Xe paradox" (Krummenacher et al. 1962). The Earth is also depleted in radiogenic Xe isotopes, i.e. I-derived ^{129}Xe and Pu- and U-derived

fissiogenic isotopes (Tolstikhin et al., 2014). Recent measurements on deep fluids and fluid inclusions trapped in Archean crustal minerals show that Xe isotopic fractionation was still occurring throughout the Archean era (Pujol et al. 2011, Avice et al. 2017). Modelling Xe degassing and re-gassing over geological times reveals that Xe recycling has been significant after 2.5-2.8 Ga (Holland and Ballentine 2006, Avice et al., 2017; Parai and Mukhopadhyay, 2018).

Xe escape from the atmosphere could explain this evolution (Pepin, 2006; Hebrard and Marty 2014, Zahnle et al., 2019). That requires either some degree of storage of Xe at depth (Pepin 2006) or the photoionization of Xe (Hebrard and Marty 2014, Zahnle 2019) providing conditions: the presence of an atmospheric organic haze and strongly nonlinear photoionization process to compensate for the weak UV flux in the Archean (Hebrard and Marty 2014), or an unlikely large amount of H_2O reduction by FeO during the Archean to provide sufficient H^+ escape flux or yet unexplained Xe escape bursts (Zahnle et al. 2019).

Alternatively, the missing Xe could be stored at depth, in the deep crust or mantle either in high *P* melts (Leroy et al., 2016) and/or minerals as shown for quartz (Sanloup et al., 2005, Crepisson et al. 2019) and olivine (i.e. Sanloup et al., 2011; Crepisson et al., 2018), or in the core (Lee and Steinle-Neumann, 2006, Zhu et al. 2014).

In the case of Mars' atmosphere, in which Xe is also depleted both in bulk element content and in light isotopes, it was proposed that I separated from Xe through a process involving water (Musselwhite and Drake, 1991) as on a chemical point of view I is hydrophilic whereas Xe is hydrophobic. Liquid water, supposed to be present at that time, would have trapped I (including ^{129}I later transformed in ^{129}Xe) while Xe was lost to space. This is the model proposed to explain that for Mars $(^{129}Xe/\ ^{132}Xe)_{Mars'satmosphere} > (^{129}Xe/\ ^{132}Xe)_{Marsmantle}$ whereas this is the opposite for

the Earth: $(^{129}Xe/^{132}Xe)_{Earth'satmosphere} < (^{129}Xe/^{132}Xe)_{MORB}$. Iodine and Xe should exhibit different behaviours during an early major water degassing event that may have occurred during the Hadean magma ocean era. ^{129}Iodine became extinct about 100 million years after the formation of the solar system. If I was degassed from the magma ocean and lost from the atmosphere together with water (Bureau et al., 2016), but not Xe, such a process would have affected the atmosphere only, and may have contributed to the isotopic atmospheric depletion in ^{129}Xe observed today. If Xe was lost together with I, magma degassing is not the process to explain its atmospheric isotopic depletion.

We test the effect of an early water degassing process of the magma ocean on a potential separation of I from Xe. For this purpose, we developed a multi-diagnostic experimental approach to measure the solubility of both Xe and I in melts using large volume presses, and monitor Xe and I partitioning between hydrous melts and aqueous fluids in situ at high pressure (P) and temperatures (T) during decompression (i.e. degassing of an ascending magma) combining diamond anvil cells experiments with synchrotron x-ray fluorescence XRF and, with Raman micro-spectroscopy devoted to measure I speciation in high P melts/fluids. We propose that Xe and I could be stored at depth, possibly in deep magma or melt layers and their cristallisation products.

2. Methods

1. Synthesis of the starting materials

Iodine and Xe bearing glasses are synthesized to obtain starting materials for diamond anvil cells experiments, and determine solubilities in high P silicate melts.

We use a natural Island Arc Basalt (IAB, basaltic sample STV301, from St Vincent volcano, Pichavant et al., 2002), relevant for subduction zones context; a natural Mid Ocean Ridge Basalt (MORB, BN06-11 from Juan de Fuca Ridge, Prouteau and Scaillet, 2013), and a synthetic haplogranite (HPG, Bureau and Keppler, 1999), a composition relevant for continental crust melts (e.g. Schmidt et al., 1997), also used as a proxy for subduction zones magmas (e.g. Bureau et al., 2003, 2010; 2016).

The IAB and MORB powders are obtained by crushing the natural lava samples. The HPG glass is prepared from a mixture of pure oxides and carbonate powders (SiO_2, Al_2O_3, Na_2CO_3, K_2CO_3). The HPG powder is dehydrated and degassed from CO_2 by a slow ramp heating from room temperature to 1200°C during 8 hours, it is melted in an atmospheric furnace for one hour at 1600°C, quenched in water, crushed and melted again and crushed to a fine homogeneous powder.

Iodine bearing glasses

To limit iron loss during experiments some platinum (Pt) capsules are doped in iron before the high *P-T* experiments. The IAB powder is loaded in open Pt capsules and melted in an atmospheric furnace at the same T and for the same duration as for the high P experiments. Capsules are then cleaned in hydrofluoric acid before being loaded and sealed. HPG and basalt powders together with NaI salt (3wt.%) are loaded in Pt capsules without or with distilled water. Pt capsules are welded and inserted either (1) in a 3.2 cm long (1/2 inch) cell-assembly composed of a graphite heater surrounded by pyrex and talc sleeves for piston cylinder experiment; or (2) in an internally heated

pressure vessel pressurized with an Ar-H_2 gas mixture (ISTO, Orléans). High *P-T* conditions of 2-3.5 GPa and 1400-1600°C are generated using the piston cylinder apparatus for 60 minutes; low *P-T* conditions of 0.2-0.4 GPa and 1300°C are generated in the internally heated pressure vessel for 240 minutes. *T* is monitored with a Type C thermocouple. The samples are quenched as glasses either by turning-off the power supply for the piston cylinder or using a fast quench device for the internally-heated pressure vessel.

Xenon bearing glasses

For glasses not doped in I, hydration is done at 2 GPa and 1400°C using a piston–cylinder apparatus with a half-inch talc pyrex assembly, a graphite heater, and dried MgO powder packed around the Pt capsule. Two hydration levels are targeted, 5 wt% and 7 wt%. The glass is sealed with the proper amount of distilled water in a Pt capsule. Xe doping is done subsequently by gas-loading in another Pt capsule partially filled with the recovered hydrous HPG glasses, and brought to 3.5 GPa and 1600°C for one hour, followed by rapid *T* quenching and decompression at room *T*. For I-Xe bearing glasses the I-glasses are Xe-doped following the same procedure. Experimental conditions are summarized in **Table 1**.

2.2 Diamond anvil cells experiments

The degassing process (*i.e.* the separation of a fluid phase from a silicate melt) is monitored *in situ*, through decompression induced by *T* decrease in Bassett-modified externally heated diamond anvil cells (DAC) equipped with *P*-driving membranes (Munsch et al., 2015). The partitioning of Xe and I between the two phases is measured *in situ* by using synchrotron XRF analysis during decompression following the same strategy as in previous studies (Bureau et al., 2010; 2016). The

DACs are equipped with large culet size (0.8 mm to 1 mm) and 2 mm thick diamonds, and externally heated by furnaces attached to both anvils. *T* is controlled by two K-type thermocouples touching each diamond anvil, and previously calibrated. The sample chamber is a 300 µm to 500 µm hole drilled in a Re gasket (initial thickness: 250 µm) compressed between the two diamonds. Observations are done along the *P* axis through the diamond anvils, and the loaded aqueous fluid is used as *P*-medium. Density of the aqueous fluid is calculated by measuring the homogenization *T* of a water vapor bubble in liquid water. Knowing the density, *P* can be calculated for a given *T* from the equation of state of the fluid phase (see Munsch et al., 2015). We obtain a *P*-range of 1.21 GPa - >1.68 GPa with a precision of 0.2 GPa for a *T*-range of 684°C - >851°C.

2.3 In situ SXRF

Synchrotron XRF quantitative analysis is performed at the beamline P02.2, Petra III (DESY, Hamburg). We use a 42.7 keV monochromatic x-ray beam focused down to 4 µm x 6 µm. For each experiment, the DAC is positioned perpendicularly to the beam, XRF spectra are detected in transmission geometry with an angle of 8° with the incident beam, with a Silicon Drift x-ray detector. Iodine and Xe can be detected *in situ* in a DAC as their high Kα and Kβ Rays (*i.e.* I: $K\alpha_I$ 28.61 keV; $K\beta_I$ 32.99 keV, Xe: $K\alpha_{Xe}$ 29.78 keV; $K\beta_{Xe}$ 33.62 keV) are not absorbed by the 2 mm thick diamond anvils. We use the I-Xe doped HPG glasses as magma analogues (HPGXe-C11, HPGXeI-04). For the HPG composition, the glass transition occurs at lower *T* compared to basaltic or peridotitic melts, which makes possible a study in resistive heating DAC whose *T* are limited to 1000°C in routine mode (max 1100°C). For each experiment, the sample chamber is half-filled with pieces of glass, and further loaded with pure water. When possible, *T* is increased up to total

miscibility, and then decreased by steps causing decompression; at each *T* step, co-existing aqueous fluid and silicate melt are analyzed (Bureau et al., 2010; 2016). At the very last stages of decompression, water bubbles nucleate in the melt and form fluid inclusions until the glass transition *T* is reached, compromising the analysis of the quenched glasses *in situ* in the DAC; the quenched aqueous fluid is also characterized. XRF analyses are calibrated *in situ* in the DAC at room conditions using a NIST 610 glass (e.g. Rocholl et al., 1997). For XRF analysis it is not necessary to use I- and Xe-enriched glasses as standards, because the whole NIST 610 spectrum is calibrated for multi elemental analysis using glasses containing elements with Kα ray energies close to that of I and Xe , such as Sb Ka = 25.2 keV, 405 ± 10 ppm in NIST610 (Rocholl et al., 1997).

2.4 In situ Raman spectroscopy

Raman spectra are collected *in situ* in a DAC on a Jobin Yvon® HR-460 spectrometer equipped with an Andor® CCD camera at IMPMC using the 1500 grooves/mm grating mode. Raman signal is excited using the 514.5 nm wavelength of an Ar^+ laser, delivering 300 mW focused into a 2 µm spot by a long-working distance Mitutoyo® x20 objective and collected in back-scattering geometry. Backscattered Rayleigh light is filtered with a set of holographic Notch filters. Spectral resolution is about 2.5 cm^{-1}. *In situ* measurement collection times are 60 s or 120 s per spectra in order to get reasonable signal-to-noise ratios. The DAC is loaded with pieces of HPG glass and a solution of H_2O-NaI (20 g/l), heated up to total miscibility between the aqueous fluid and silicate melt, and the first Raman measurements are performed in the supercritical fluid at 860°C. *T* is then

232 decreased, and Raman spectra are acquired after 10 min of equilibration in co-existing aqueous
233 fluid and silicate melt.

234

235 *2.5 Analyses of quenched samples*

236 Quenched glasses from large volume press and DAC experiments are recovered, mirror polished
237 (except for DAC samples) for *ex situ* scanning electron microscopy, electron microprobe and ion
238 beam analyses. We use a Zeiss Ultra 55 filed emission scanning electron microscope (IMPMC)
239 with a working distance between 3 mm and 7.5 mm, and a voltage of 15 kV to observe crystal-free
240 glasses texture. Major elements are analyzed using a Cameca SX FIVE electron microprobe at
241 CAMPARIS facility (Sorbonne Université). Acceleration voltage is set to 15 kV, current to 4 nA
242 and beam is focused to 15 µm diameter at the surface of the sample. Counting times are 10 s per
243 element on both peak and background. We use two internal standards (EtC, Bureau et al., 2000 ;
244 KE12, Bureau and Metrich, 2003). About 10 to 30 analyses are performed for each sample. Major
245 elements compositions for recovered high P-T samples and starting glasses are listed in **Table 2**.

246 Particle induced x-ray emission (PIXE), Rutherford backscattering spectrometry (RBS) and Elastic
247 Recoil Detection Analysis (ERDA) are performed at the nuclear microprobe, CEA Saclay NIMBE
248 / LEEL. Samples are analyzed by PIXE for I and Xe. The 3x3 μm^2 proton beam of 2 MeV, 600 pA
249 is scanned on large areas (250 x 250 μm^2 to 50 x 50 μm^2) during one to a few hours, corresponding
250 to deposited charges ranging from 0.6 µC to 2.4 µC. Emitted x-rays are collected using a Silicon-
251 drift x-ray detector. Simultaneous RBS analysis allows to check the major element compositions
252 of the glasses, and to map fluid inclusions trapped in the glass. Elemental maps are processed in
253 order to select the areas of interest (e.g. bubble-free glass areas). Concentrations are obtained as

described in Bureau et al. (2010, 2016). Data analysis is calibrated with the NIST 610 Glass, including the calibration of the PIXE solid angle done on Sb Lα line at 3.44 keV (Sb content = 405 ± 10 ppm). The quantification process is cross-checked using the well-known reference glasses EtC and KE12. To quantify I content of HPG glasses, we use the Lα (3.92 KeV) and Lβ rays (4.22 KeV), both rays giving similar concentrations (**Table 2**). To quantify the I content of basaltic glasses, we use only the Lβ lines due to interferences between the I Lα line at 3.94 keV and the calcium Ca-Kβ line at 3.69 keV (**Figure 1**). To quantify Xe in all glasses, we use the Lα line at 4.1 keV.

Water contents are obtained by ERDA, a technique based on the detection of protons after their ejection from the samples through elastic collisions at a grazing angle of 15° induced by a ^{4}He 4x16 μm^2 incident beam of 3 MeV. RBS measurements are performed using an annular detector positioned at 170° with respect to the incident beam direction in order to monitor the charge delivered to the sample, necessary to allow hydrogen quantification. Details about the procedure can be found in Bureau et al (2009).

3. Results

3.1 I-Xe doped Glasses

All glassy samples are chemically homogeneous with respect to major elements, water, and I thus attesting that chemical equilibrium was reached. For the samples of HPG composition synthesized at 0.4 GPa, we observe large I-rich bubbles, that are excluded from the maps for PIXE data processing. The presence of I-rich water bubbles may be due to the fact that at this *P* condition, water solubility in HPG melts is lower than the initial amount of water loaded in the capsule (> 5 wt.% at 0.2 GPa, 800°C, Holtz et al., 1992), water and I degas simultaneously during decompression (Bureau et al., 2016). Bubbles are not observed in samples of IAB composition as we use initial water contents (< 2 wt.%) lower than the solubility of water in basalts at high *P* (up to 8 wt% H_2O at 0.4 GPa, Sisson and Grove 1993). Xe-doped glasses also exhibit large bubbles due to Xe oversaturation from the gas loading system.

Iodine contents range from 0.46±0.07 wt.% I to 1.33±0.15 wt.% I (in the presence of Xe) in both hydrous HPG, and from 0.48±0.07 wt.% to 2.97±0.58 wt.% I for IAB. At 3.5 GPa (see below), there is no excess I, added at the level of 2.54 wt.% I (3 wt.% NaI) in the starting material. This suggests that the solubility at 3.5 GPa may exceed 2.97 wt.%. Solubility expresses the ability of a solute to dissolve in a solvent; it is given by the maximum concentration of the solute in a solvent at equilibrium. Therefore we measured I solubility only for experiments performed up to 2 GPa.

These concentrations are much higher than the I content measured in basaltic volcanic glasses, usually a few ppb to a few hundreds of ppb (i.e. Schilling et al., 1980; Déruelle et al., 1992; Kendrick et al., 2012). We observe a positive trend between I content and *P* for the basaltic composition (**Figure 2A**), similar to that observed for the solubility of chlorine (Webster, 1997) and bromine (Bureau and Métrich, 2003) in hydrous melts in the absence of aqueous brines and/or

hydrosaline fluids (see Webster and Mandeville 2007). For *P* up to 2 GPa, I solubility values in silicate melts are comparable to those of chlorine and bromine (**Figure 2C**). Because the amount of I dissolved in the basaltic melt at 3.5 GPa (i.e. 2.97±0.58 wt.% and 2.67±0.58 wt.%) is equal to the initial amount loaded in the starting sample (about 2.54 wt.%) the melts may not be saturated with respect to I at these high *P*, which means that I solubility is probably higher than 2.97 wt.% for $P > 3.5$ GPa. The Fe content of the samples is variable due to Fe loss to the Pt capsules (1.05 wt.% to 8.51 wt.% FeO). Even experiments performed at high *P* (2 GPa and 3.5 GPa) and *T* (1400-1600°C) with Fe-doped Pt capsules do not prevent partial Fe loss from the silicate melt (see samples BA-PC88 and BA-PC89, respectively at 1.75 wt.% and 5.77 wt.% FeO while sample BA-C7 synthesized at 0.2 GPa-1300°C exhibits the right FeO content at 8.51 wt.%). Because the initial water content is not equivalent for all samples we cannot discuss potential relationship between I and water contents.

The Xe solubility value at 3.5 GPa is much higher for HPG than for basalts: 4 wt.% for HPG falling down to 0.4 wt.% for IAB and to 0.27 wt.% for MORB (Figure 2B), in agreement with data for tholeiitic melts (Schmidt and Keppler, 2002).

Two experiments are performed for basaltic compositions doped in both Xe and I at 3.5 GPa (**Table 2**), i.e. IAB (BA-PC73 1.81 wt.% I, 0.19 wt.% Xe) and MORB (BM-PC73 2.00 wt.% I, 0.33 wt.% Xe). These concentrations are slightly lower than for experiments performed in the presence of a single element. **Figure 2A** and **2B** summarize Xe and I concentrations at saturation conditions with respect to *P*. Both Xe and I solubility increase with *P* in melts, I solubility is possibly affected by the composition of silicate melts, which remains to be tested by structural studies, while Xe solubility is 10-fold higher in HPG than in basalts. However, such high concentrations are not expected in natural rocks, in the view of their very low terrestrial abundances.

3.2. In situ high P-T partition coefficients of iodine and xenon between melts and fluid

Xe and I concentrations measured *in situ* at high *P* and *T* in melts and fluids (SXRF), *ex situ* in glassy phases (PIXE) along with calculated partition coefficients are reported in **Table 3**. *Ex situ* data illustrate the crucial need of *in situ* data, due to strong Xe and I degassing during decompression in the aqueous phases that produces Xe-I-rich bubbles (**Figure 3**) and modifies dramatically the I and Xe concentration in quenched glasses compared to the silicate melts. If remaining in the glass I content is too low to be detected. Therefore, in the present case the analysis of both phases is necessary (silicate melt and aqueous fluid), as illustrated in the SXRF spectra presented in **Figure 4**. For experiment #02, the quantification of Xe in the supercritical fluid allows mass balance calculation, at high *P:* 45% melt and 55% aqueous fluid.

These partitioning experiments are performed between two phases, they differ from solubility experiments performed for a single phase. The presence of a water phase in the system strongly modifies the behaviour of both Xe and I in the silicate melt, the concentrations of these elements measured in aqueous fluids and in water-saturated silicate melts, in equilibrium with each other, cannot be compared with the solubility values measured in glasses quenched from high *P-T* liquid silicates.

For a *P* range of 1.64 GPa to 1.22 GPa and a *T* range from 860 °C to 650 °C, $D^{Xe}_{f/m}$ ranges from 0.15 to 2748 (including Xe-I doped experiments), while I partitioning could only be measured at

1.5 GPa and 794°C with $D^{I}_{f/m}$ = 0.97 (**Figure 5**). Partition coefficients increase with decreasing *P*, implying strong degassing processes for both Xe and I. The comparison with previous results for I, i.e. $D^{I}_{f/m}$ from 1.92 to 41, at *P* from 1.8 GPa to 0.1 GPa (Bureau et al., 2016) shows that Xe is more efficiently lost from the silicate melt during decompression than I. A relationship is observed between the partitioning of Xe and its melting curve as shown in **Figure 6**, where the melting curve is presented together with the *P*-*T* conditions for each experiment. For experiment #02, the first partition coefficient ($D^{Xe}_{f/m}$ 0.15 at 851°C-1.68 GPa) was measured 10°C below total miscibility conditions (i.e. when the silicate melt and aqueous fluid separate from a single supercritical fluid). For that experiment only the $D^{Xe}_{f/m}$ is below unity at 0.15, which implies more Xe dissolved in the melt than exsolved. It is observed in **Figure 6** that the *P*-*T* conditions of this experiment fall close to the melting curve of Xe, while those of all other experiments are below this curve, and correspond to situations where Xe is largely dominant as a fluid phase ($D^{Xe}_{f/m}$ >>1). It shows that the exsolution of Xe from the silicate melt during both decompression and decrease of *T* is not promoted by the water phase as is the case for I (highly hydrophilic, Bureau et al., 2016), but is only determined by the *P*-*T* conditions, in other words by the melting of Xe that is *P*-*T* dependent. This observation is consistent with previous reports of Xe retention in silicates occurring systematically above the melting curve of Xe (Sanloup et al. 2005, Sanloup et al. 2011, Crépisson et al. 2019), a reaction likely driven under *P* by the important volume reduction between the reactants (i.e. silicates and molten Xe with a consequently large molar volume) and the product (i.e. Xe-doped silicates).

3.3. Iodine speciation in hydrous silicate melts

In situ Raman measurements are performed in the supercritical fluid enriched with respect to I at 860°C, and in the melt and aqueous fluid in equilibrium close to miscibility at 850°C and 1.5 GPa (**Figure 7**). We observe a Raman band at about 134 cm^{-1} in the aqueous fluid at both room and high *P-T* conditions, that progressively also appears in the HPG silicate melt albeit with a smaller intensity close to miscibility conditions, and in the single fluid resulting from total miscibility. We attribute this band to I species. The 110-174 cm^{-1} range is indeed known to correspond to I-I bond stretching vibration of polyiodides moieties in aqueous solutions, as the Raman band at 180 cm^{-1} for solid I_2 is expected to move towards lower frequencies when di-I interacts with donors to form complexes (Deplano et al., 1999). We do not observe oxidized I species (IO^{3-}) at 779 cm^{-1} (Shen et al., 1937). Spectroscopic data agree well with *in situ* partitioning measurements of Figure 6, showing a transfer of I to the aqueous fluid ($D^{I}_{f/m} > 1$) when both *P* and *T* decrease.

4. Discussion

4.1 Iodine and Xenon in silicate melts

We measured I solubility in silicate melts from various settings (deep continental crust, subduction zone). Iodine contents for quenched hydrous glasses are up to 1.33±0.15 wt.% at 3.5 GPa in HPG, and up to 1.42±0.23 wt.% at 2 GPa for IAB. In all cases we show that I can be significantly incorporated in the silicate networks, meaning that I may be locally enriched in silicate melts at depth. This may have consequences on the real I content of the bulk silicate Earth that is believed

to be very low, based on measurements performed in basalts recovered at ambient conditions (McDonough and Sun, 1995).

We measured Xe solubility in silicate melts at 3.5 GPa for both HPG (up to 4 wt.% Xe) and basalts (tholeiites 0.4wt.%, Arc basalts 0.27 wt.% Xe), in agreement with data on tholeiitic melts from Schmidt and Keppler (2002). All results show that the amount of Xe dissolved in high *P* melts at depth may be significant, provided that *P* and *T* conditions remain above Xe melting curve. It is also observed that Xe and Ar have similar solubility values in wt% in silicate melts (this study, Leroy et al., 2018, Schmidt and Keppler 2002). The high solubility of Xe in HPG melts was shown to be due to Xe insertion in the melt ring structure (6-membered rings) through the formation of Xe-O bonds (Leroy et al., 2018), it is suggested that the same process may be at stake for basaltic melts that have much less 6-membered rings than polymerized silica-rich melts such as HPG, and a consequently much lower Xe solubility. The incorporation of Xe through *P*-induced oxidation process in the melt differs from the incorporation of I through I-I bonds of polyiodides, and/or potentially associated to alkali cations.

The *in situ* monitoring of Xe and I behaviours in fluids at conditions analogous to magma degassing show that degassing of I and Xe from silicate melts to the aqueous fluid involve different processes. I is decoupled from Xe because it systematically degasses with water (forming I_2 moieties in the aqueous fluid), while Xe only degasses if its retention in the silicate melt is not thermodynamically favored. Similarly, mantle re-gassing processes at subduction zones could be different for both elements (see 4.3). We note a slope change in the pressure evolution in $D^{I}_{f/m}$ circa 0.5 GPa, flattening at $D^{I}_{f/m} = 4$; it might relate to a change of retention mechanism of iodine in the silicate melt as reported for bromine under pressure (Cochain et al., 2015).

405

406

407 *4.2 Iodine and Xenon in subduction zones*

408

409 Although I is present at the ppb level in igneous rocks, the potential content of I in silicic melts and
410 natural basaltic melts at high *P* can reach a few weight percent, similarly to bromine. This may
411 have important consequences in subduction zones.

412 About 70% of the I present in the crust is believed to originate from sea water sediments of organic
413 origin, indicating potentially a significant recycling of I to the mantle. I mobility in subduction
414 zones is believed to be promoted by the dehydration of serpentinites, because serpentines have the
415 ability to significantly incorporate I (John et al., 2011).
416 When subducted with marine sediments, part of I is mobilized in fluids and released in brines from
417 the forearc areas, together with I from old organic-rich marine formations located in the upper plate
418 of the forearc regions (i.e. Japanese forearc, Tomaru et al.; 2007). Volcanic gases and forearc fluids
419 from subduction zone volcanoes are enriched in I with respect to other settings, as for example the
420 Central American volcanic arc (Witt et al., 2008) or in Japan (Tomaru et al.; 2007). The abundance
421 of I found in the volcanic arc material may therefore be controlled by fluid release from
422 deserpentinizing slab mantle, a conclusion also supported by the analysis of I in back-arc basin
423 basalts (Kendrick et al., 2012). The high solubility of I in natural basaltic melts reported here
424 indicates that most of I released from serpentinites can be incorporated in magmas formed in the
425 mantle wedge. The first melt produced in the slab at typical *T* for sub-arc depths are silica-rich with
426 high alkali contents such as HPG (e.g. trondhjemites, Prouteau & Scaillet, 2013), possibly enriched

in I. Iodine volcanic injection to the atmosphere is potentially having significant consequences on the stratospheric ozone chemistry (Bureau et al., 2000).

While the major part of I present in subducted slabs is reinjected to the atmosphere, another part may be transported at depth in slabs. This is in agreement with the study of intraplate mantle xenoliths from various settings, some of them exhibiting I/Cl ratios more than one order of magnitude higher than the mantle value. It is proposed that I may be transported into the mantle at least beyond sub-arc depth (Kobayashi et al., 2019). This constrains the amount of subducted I into the convecting mantle to a few % of the subduction input. A deep storage of I is in agreement with the presence of I-rich aqueous fluid inclusions in lithospheric diamonds (Burgess et al., 2002), with the high halogen concentrations of the de-serpentinized harzburgite residues from serpentine breakdown, that are returned to the deep mantle (John et al., 2011) or in the seawater-derived I preserved in exhumed mantle wedge peridotite (Sumino et al., 2010). The processes suggested from our preliminary results may be migration and storage in deep melts.

We show the appearance of polyiodides moieties in hydrous silicate melt and supercritical fluid at 850°C and >1.5 GPa pressure. In a recent study of bromine in high *P* hydrous melts of HPG composition, Cochain and co-workers (2015) show that significant amounts of Br (up to 2.2 wt.%) can be retained in silicate melts at 3.4 GPa in the presence of water (up to 4.4 wt.%). They observe a change of Br coordination shell from a $Br[Na_x(H_2O)_y)]$ complex at low *P* to an alkali structure at high *P* (at least from 2 GPa on although it remains to be investigated at lower *P*), whereby Br is surrounded by two oxygens at 1.9 Å and a mean of 6.6 Na atomes at 3.7 Å. A similar process may occur for I at high *P*, allowing a storage at depth in hydrous high *P* melts.

Xenon is also believed to be significantly recycled in the mantle (e.g. Holland and Ballentine 2006; Parai and Mukhopadhyay, 2018). Different processes are involved for I and Xe “ingassing” of the

mantle. During slab dehydration, a significant part of I would be efficiently washed out from the slab by aqueous fluids, and degassed back to the surface, while Xe is also recycled through aqueous fluids (**Figure 6**) but then it would remain in the mantle where it is expected to be stored in deep silicate melts/minerals. The recent examination of noble gases (including Xe) and halogens in serpentinites and secondary peridotites illustrates the key role played by serpentinites and other equivalent metamorphosed minerals where all these elements are progressively less abundant during dehydration processes and then recycled in the mantle (Kendrick et al., 2018). For Xe and possibly I, en route to the deep Earth, successive incorporations in mineral lattices and silicate melts may occur such as at the boundary between the transition zone and the lower mantle during dehydration melting process (Schmandt et al., 2014).

4.3. The depletion in light xenon of the Modern Earth's atmosphere and the missing xenon

The monitoring in real time of I and Xe partitioning during conditions analogous to magma ascent reveals two distinct behaviours. I is efficiently washed out of the silicate melt by water ($D^{I}_{f/m} >> 1$ see Bureau et al., 2016). Xenon is lost from the silicate melts much more significantly ($D^{Xe}_{f/m}$ up to 2748) but only below its melting curve. Water can therefore not be involved in the depletion in light Xe of the Modern Earth's atmosphere, except in the eventuality of deep hydrous fluids trapping I, implying a deep storage of ^{129}Xe, daughter isotope of ^{129}I, that would cause an increased ($^{129}Xe/ ^{132}Xe$) ratio in mantle partial melts (MORB). If the Early Earth was wet, both elements should have been totally degassed from the upper magma ocean, and potentially from the whole

magma ocean through effective mixing by convection. Fractional crystallization processes are proposed to account for the missing Xe, Xe can be stored in olivine up to 0.4 wt.% (Crepisson et al., 2018) through Si substitution in the olivine lattice and consequent oxidation of Xe, such as observed in high *P* melts (Leroy et al., 2018). Fractional crystallization of the magma ocean may have separated I from Xe by keeping Xe in minerals at depth while I (including ^{129}I) is concentrated in the melt and later lost to space.

In the current day Earth both I and Xe, can be stored in supercritical fluids if the *T* is high enough. Xe can be efficiently stored in deep crustal melts (i.e. very high Xe solubility in haplogranitic melts) and in the mantle, and/or in melt layers, such as at the lithosphere asthenosphere boundary (Crépisson et al., 2014), at 350 km depth (Tauzin et al., 2010), at the top of the transition zone at 410 km depth or below the TZ at 660 km depth (Schmandt et al. 2014), at the core mantle boundary CMB (Labrosse et al., 2007). This would contribute to the "missing Xe" and would imply a significant storage of I at depth, questioning in turn our knowledge of the abundance of I in the bulk silicate Earth.

Conclusions

We have studied Xe and I behaviour at magmatic conditions, from room conditions up to 3.5 GPa and 1600°C, and under hydrous conditions for two magmatic systems, haplogranite (magma analogue for silicic melts) and basalts (MORB and IAB). We show that both elements reach high solubilities at high *P*, albeit with a strong composition dependence for Xe only. This strongly

contrasts with the low abundances of these elements in mantle products. Results illustrate that despite the proximity of Xe and I in the periodic table, their respective behaviour in silicate melts involve different mechanisms. I is incorporated as polyiodides (I-I bonds) while Xe is oxidized at depth (Xe-O bonds, Leroy et al., 2018). The *in situ* monitoring of shallow water degassing process reveals that both elements totally degas during decompression, but while water enhances the degassing of I, it has not effect on the degassing of Xe. Instead Xe degassing is strongly T-dependent with a partition coefficient one order of magnitude higher than for I at low *T*, but lower than unity below the Xe melting curve. Water can therefore not be involved in the depletion in light Xe of the Modern Earth's atmosphere, except for deep aqueous fluids in the eventuality of a deep storage, at conditions below the Xe melting curve. Storage of Xe in deep melt layers melts layers, such as at the lithosphere-asthenosphere boundary, or deeper, may account for the missing Xe, possibly associated to fractional crystallization processes as Xe incorporation in olivine can be significant (up to 0.4 wt.%, Crepisson et al., 2018).

Iodine is not expected to enter the lattice of nominally anhydrous phases, it is concentrated in silicate melts, causing the separation of ^{129}I (later ^{129}Xe) from Xe. Deep silicate melts may favour the storage of I (and Xe) in the bulk silicate Earth, either upon early Earth's differentiation or upon modern recycling at subduction zones. The high capability of magmas to incorporate I at depth and to degas I during ascent in subduction zones is also a potential significant source of I for the atmosphere, an output that still lacks quantification today.

Acknowledgements

We thank the staff from the nuclear microprobe of LEEL, CEA Saclay, and Rémi Champallier from ISTO for their help during the course of this research. Portions of this research were carried out at the light source PETRA III at DESY, a member of the Helmholtz Association (HGF). We thank Michel Fialin for assistance with the electron microprobe analysis, Imène Estève for assistance with the scanning electron microscopy, and Etienne Balan for fruitful discussion. We acknowledge the Editor, Tamsin Mather, and two anonymous reviewers for their constructive reviews. The SEM facility of IMPMC is supported by Région Ile de France Grant SESAME 2006 NOI-07-593/R, INSU-CNRS, INP-CNRS, UPMC, and by the French National Research Agency (ANR) Grant ANR-07-BLAN-0124-01. The research leading to these results has received funding from the European Community's Seventh Framework Programme (FP7/2007-2013) under grant agreements no. 312284 and 259649 (European Research Council starting grant to C.S.), from the EGIDE PHC PROCOPE (project 26673WC to H.B.), and from French state funds managed by the ANR within the Investissements d'Avenir programme under reference ANR-11-IDEX-0004-02.

References

Anders, E., and Owen, T. (1977) Mars and Earth : origin and abundances of volatiles, Science 198, 453-465.

Armytage, R.M.G., Jephcoat A.P., Bouhifd, M.A., Porcelli, D. (2013) Metal-silicate partitioning of iodine at high pressures and temperatures: implications for the Earth's core and 129Xe budgets. Earth and Planet. Sci. Let. 373, 140-149.

Avice, G., Marty, B., Burgess, R. (2017) The origin and degassing history of the Earth's atmosphere revealed by Archean Xenon. Nature Comm. DOI 10.1038/ncomms15455.

Avice, G., and Marty, B. (2014) The iodine-plutonium-xenon age of the Moon-Earth system revisited. Phil. Trans. Of the Royal Soc. A372 :20130260.

Belonoshko A.B., Davis S., Rosegren A., Ahuja R., Johansson B., Simak S.I., Burakovsky L., Preston D.L. (2006) Xenon melting: Density functional theory versus diamonod anvil cell experiments. Phys. Rev. B 74, 054114.

Bureau H. and Keppler H. (1999). Complete miscibility between silicate melts and hydrous fluids in the upper mantle: experimental evidence and geochemical implications. Earth and Planetary Science Letters, **165**, 187-196.

Bureau, H., Keppler, H., Métrich, N., (2000). Volcanic degassing of bromine and iodine: experimental fluid/melt partitioning data and applications to stratospheric chemistry Earth and Planet. Sci. Let. **183**, 51-60.

Bureau, H., Métrich, N., (2003). An Experimental Study of Bromine Behavior in Water-Saturated Silicic Melts, Geochimica et Cosmochimica Acta, vol **67/9**, 1689-1697.

Bureau, H., Raepsaet, C., Khodja, H., Carraro, A., Aubaud, C. (2009) Determination of hydrogen content in geological samples using Elastic Recoil Detection Analysis (ERDA). Geochimica et Cosmochimica Acta, 73,3311-3322.

Bureau, H., Foy, E., Raepsaet, C., Somogyi, A., Munsch, P., Simon, G., Kubsky, S., (2010). Bromine cycle in subduction zones through in situ br monitoring in diamond anvil cells Geochim. Cosmochim. Acta, **74**, 3839-3850.

Bureau, H., Auzende, A.-L., Marocchi, M., Raepsaet, C., Munsch, P., Testemale, D., Mézouar, M., Kubsky, S., Carrière, M., Ricolleau, A., Fiquet, G. (2016) Modern and past volcanic degassing of Iodine, Geochimica et Cosmochimica Acta, 173, 114-125.

Burgess R., Layzelle E., Turner G. and Harris J. W. (2002) Constraints on the age and halogen composition of mantle fluids in Siberian coated diamonds. Earth and Planet Sci. Lett.**197**, 193–203.

Clay P.L., Burgess, R., Busemann H., Ruzié-Hamilton L., Joachim B., Day J.M.D., Ballentine C. (2018). Halogens in chondritic meteorites and terrestrial accretion. Nature 551, 614-618.

Cochain, B., Sanloup, C., De Grouchy, C., Crepisson, C., Bureau, H., Leroy, C., Drewitt, J., Kantor, I., Irifune, T. (2015) Bromine speciation in hydrous silicate melts at high pressure. Chemical geology 404, 18-26.

Crépisson, C., Morard, G., Bureau, H., Prouteau, G., Morizet, Y., Petit-Girard, S., Sanloup, C., (2014) Magmas trapped at depth and the continental lithosphere-asthenosphere boundary, Earth and Planetary Science Letters, 393, 105-112.

Crepisson, C., Blanchard, M., Lazzeri, M., Balan, E., Sanloup, C., (2018). New constraints on Xe incorporation mechanisms in olivine from first-principles calculations, Geochim. Et Cosmochim. Acta, **222**, 146-155.

576 Deplano, P., Ferrarro, J.R., Mercuri, M.L. Trogu, E.F., (1999) Structiral and Raman spectroscopic
577 studies as complementary tools in elucidating the nature of the bonding in polyiodides and in
578 donor-I_2 adducts. Coord. Chem Rev. 188, 71-95.

579 Déruelle, B., Dreibus, G., Jambon, A., (1992). Iodine abundances in oceanic basalts: implications
580 for Earth's dynamics. Earth and Planet. Sci. Let. **108**, 217-227.

581 Fehn U., (2012). Tracing crustal fluids: Applications of Natural ^{129}I and ^{36}Cl. Annu. Rev. Earth
582 Planet. Sci. **40**:45–67.

583 Hebrard, E., and Marty, B. (2014) Coupled noble gas-hydrocarbon evolution of the Early Earth
584 atmosphere upon solar irradiation. Earth and Planet. Sci. Let. 385, 40-48.

585 Holland, G., Ballentine, C.J. (2006) Seawater subduction controls the heavy noble gas
586 composition of the mantle. Nature, 441, 186-191.

587 Holtz, F., Behrens, H., Dingwell, D.B., Taylor, R. (1992) Water solubility in aluminosilicate melts
588 of haplogranite composition at 2 kbars. Chemical Geology, 96, 289-302.

589 John, T., Scambelluri, M., Frische, M., Barnes, J.D., Bach, W., (2011). Dehydration of subducting
590 serpentinite: Implications for halogen mobility in subduction zones and the deep halogen cycle
591 Earth and Planet. Sci. Let. **308**, 65-76.

592 Johnson, L.H., Burgess, R., Turner, G., Milledge, H.J., Harris, J.W., (2000). Noble gas and halogen
593 geochemistry of mantle fluids: comparison of African and Canadian diamonds. Geochim.
594 Cosmochim. Acta, **64**, 717-732.

595 Kendrick, M.A., Woodhead, J.D., Kamenetsky, V.S., (2012). Tracking halogens through the
596 subduction cycle, Geology, **40**, 1075-1078.

597 Kendrick M.A., Scambelluri, M., Hermann, J., Pardon-Navarta, J.A. (2018) Halogens and noble
598 gases in serpentinites and secondary peridotites: implications for seawater subduction and the
599 origin of mantle neon. Geochimica et cosmochimica Acta, 235, 285-304.

600 Kobayashi, M., Sumino, H., Burgess, R., Nakai, S., Iizuka T., Nagao, J., Kagi, H., Nakamura, M.,
601 Takahashi E., Kogiso, T., Ballentine, C.J. (2019) Halogen heterogeneity in the lithosphere and
602 evolution of mantle halogen abundances infreed from intraplate mantle xenoliths. Geochemistry,
603 Geophysics, Geosystems, 20, 952-973.

604 Krummenacher, D., Merrihue, C.M., Pepin, R.O., Reynolds, J.H. (1962) Meteoric krypton and
605 barium versus the general isotopic anomalies in meteoritic xenon. Geochim. Et Cosmochim. Acta
606 26, 231-249.

607 Labrosse, S., Hernlund, J.W., Coltice, N. (2007), A crystallizing dense magma ocean at the base
608 of the Earth's mantle. Nature 450, 866- 869.

609 Lee K. K. M. et Steinle-Neumann G. (2006) High-pressure alloying of iron and xenon: « Missing
610 » Xe in the Earth's core? J. Geophys. Res. Solid Earth 111, 1-7.

611 Leroy, C., Sanloup, C. Bureau, H., Schmidt, B.C., Konôpkova, Z., Raepsaet, C. (2018) Bonding of
612 xenon to oxygen in magmas at depth. Earth and Planetary Sciences Letters 484, 103-110.

613 Marty, B., (2012). The origins and concentrations of water, carbon, nitrogen and noble gases on
614 Earth. Earth and Planet. Sci. Let. **313-314**, 56-66.

615 McDonough, W.F., Sun, S.S., 1995. The composition of the Earth. Chem. Geol. 120, 223-253.

616 Munsch P., Bureau H., Yakoubi M. El, Khodja H. et Zaitsev A. (2015) The use of 13C diamond as
617 pressure and temperature sensor for diamond-anvil-cell experiments. Eur. J. Mineral. 27, 365-375.

618 Musselwhite D.S., Drake, M.J., Swindle T.D. (1991) Early outgassing of Mars supported by
619 differential water solubility of iodine and xenon. Nature, 352, 697-699.

620 Ohtani, E., (2005). Water in the mantle, Elements, **1**, 25-30.

621 Ozima, M., and Podosek, F.A. (1999) Formation age of Earth from $^{129}I/^{127}I$ and $^{244}Pu/^{238}U$
622 systematics and the missing Xe. J. of Geophys. Res. 104, 25493-25499.

623 Parai, R., Mukhopdhyay, S. (2018) Xenon isotopic constraints on the history of valotile recycling
624 into the mantle. Nature 560, 223-227.

625 Pepin, R.O., (2006) Atmospheres on terrestrial planets: clues to origin and evolution. Earth and
626 Planet. Sci. Lett. 252, 1-14.

627 Pichavant M., Mysen B. O. and Macdonald R. (2002) Source and H2O content of high-MgO
628 magmas in island arc settings: An experimental study of a primitive calc-alkaline basalt from St.
629 Vincent, Lesser Antilles arc. Geochim. Cosmochim. Acta 66, 2193–2209.

630 Pujol, M., Marty, B., Burgess, R., (2011) Chondritic-like xenon trapped in Archean rocks: a
631 possible signature of the ancient atmosphere. Earth and Planet. Sci. Lett. 308, 298-306.

632 Prouteau G., Scaillet B. (2013) Experimental Constraints on Sulphur Behaviour in Subduction
633 Zones: Implications for TTG and Adakite Production and the Global Sulphur Cycle since the
634 Archean. J. Petrol. 54, 183-213.

635 Rodriguez-Vargas, A., Koester, E., Mallmann, G., Conceiçao, R.V., Kawashita, K., Weber, M.B.I.
636 (2005) Mantle diversity beneath the Colombian Andes, Northern volcanic zone: Constraints from
637 Sr and Nd isoptopes. Lithos 82, 471-484.

638 Sanloup C., Schmidt B.C., Chamorro Perez E.M., Jambon A., Gregoryanz E., Mezouar M. (2005)
639 Retention of Xenon in Quartz and Earth's missing Xenon. Science 310, 1174-1177.

Sanloup, C., Schmidt, B. C., Gudfinnsson, G., Dewaele, A., Mezouar, M., (2011). Xenon and argon: a contrasting behavior in olivine at depth. Geochim. Cosmochim. Acta 75, 6271-6284.

Schilling, B.G., Bergeron, M.B., Evans, R., (1980). Halogens in the mantle beneath the North Atlantic. Phil. Trans. R. Soc. Lond. **A 297**, 147-178.

Shen, S.T., Yao, Y.T., Wu, T.-Y. (1937) Depolarization of Raman lines and structure of chlorate, bromate and iodate ions. Phys. Rev. 51, 235-238

Shinohara, H., (2009). A missing link between volcanic degassing and experimental studies on chloride partitioning. Chemical Geology, **263**, 51-59.

Schmandt, B., S. D., Jacobsen, T. W., Becker, Z. X., Liu, K. G,. Dueker, 2014. Dehydration melting at the top of the lower mantle. Science, 344, 1265-1268.

Schmidt B. C. et Keppler H. (2002) Experimental evidence for high noble gas solubilities in silicate melts under mantle pressures. Earth Planet. Sci. Lett. 195, 277-290.

Schmandt, B., Jacobsen, S.D., Becker, T.W., Liu, Z.X., Dueker, K.G., 2014. Dehydration melting at the top of the lower mantle. Science344, 1265–1268.

Schmidt, B.C., Holtz, F., Scaillet, B., Pichavant, M. (1997). The influence of H2O-H2 fluids and redox conditions on melting temperatures in the haplogranite system. Contrib. Mineral. Petrol. 126, 386-400.

Sisson, T.W., Grove, T.L., (1993) Experimental investigation of the role of H_2O in calc-alkaline differenciation and subduction zone magmatism. Contrib. Mine. Petro. 113, 143-166

Snyder, G.T., Savov, I.P., and Muramatsu, Y., (2005). Iodine and boron in Mariana serpentinite mud volcanoes (ODP Legs 125 and 195): implications for forearc processes and subduction recycling. *In* Shinohara, M., Salisbury, M.H., and Richter, C. (Eds.), Proc. ODP, Sci. Results, **195**, 1–18

Sumino, H., Burgess, R., Mizukami, T., Wallis, S.R., Holland, G., Ballentine, C.J., (2010). Seawater-derived noble gases and halogens preserved in exhumed mantle wedge peridotite. Earth and Planet. Sci. Let. **294**, 163-172.

Tauzin, B., Debayle, E., Wittlinger, G. (2010). Seismic evidence for a global low-velocity layer within the Earth's upper mantle. Nature Geoscience 3, 718-721.

Tomaru, H., Ohsawa, S., Amita, K., Lu, Z., Fehn, U. (2007). Influence of subduction zone settings on the origin of forearc fluids: Halogen concentrations and $^{129}I/I$ ratios in waters from Kyushu, Japan. Applied Geochemistry, 22, 676-691.

Tolstikhin, I., Marty, B., Porcelli, D., Hofmann, A. (2014) Evolution of volatile species in the Earth's mantle : A view from xenology, Geochim et Cosmochim. Acta 136, 229-246.

Webster, J.D., 1997. Chloride solubility in felsic melts and the role of chloride in magmatic degassing, Journal of Petrology, 38, 1793-1807.

675 Webster J. D. and Mandeville C. W. (2007) Fluid Immiscibility in Volcanic Environments. Rev.
676 Mineral. Geochemistry 65, 313‑362.

677 Williams, Q., and Garnero, E. J., (1996). Seismic evidence for partial melt at the base of the Earth's
678 mantle. Science 273, 1528–1530.
679
680 Witt, M.L., Mather, T.A., Pyle, D.M., Aiuppa, A., Bagnato, E., Tsanev, V.I., (2008). Mercury and
681 halogen emissions from Massaya and Telica volcanoes, Nicaragua. Journal of Geophysical
682 Research, **113**, B06203.
683
684 Zahnle, K.J., Gacesa, M., Cartling, D.C. (2019) Strange messenger: A new history of hydrogen on
685 Earth, as told by Xenon. Geochimica et Cosmochimica Acta, 244, 56-85
686

687 **Table 1: Experimental conditions**
688

Sample	P (GPa) (±0.05GPa)	T (°C) (±50°C)	Duration (min)	Starting materials	Description
HPGI-03	0.4	1300	240	HPG + NaI + H_2O	internally heated pressure vessel
HPGI-05	0.4	1300	240	HPG + NaI + H_2O	internally heated pressure vessel
HPGXe-02	3.5	1400	60	HPG + Xe + H_2O	Piston cylinder
HPGXe-C11	3.5	1600	60	HPG + Xe + H_2O	Piston cylinder
HPGXe-C17	3.5	1400	240	HPG + Xe + H_2O	Piston cylinder
HPGXe-C6	3.5	1400	240	HPG + Xe + H_2O	Piston cylinder
HPGXeI-04	3.5	1600	240	HPG + Xe + NaI + H_2O	Piston cylinder
BA-C7	0.2	1300	240	STV301 + NaI + H_2O	internally heated pressure vessel
BA-PC82	3.5	1600	60	STV301 + NaI + H_2O	Piston cylinder
BA-PC83	3.5	1600	60	STV301 + NaI + H_2O	Piston cylinder
BA-PC87	2	1400	60	STV301 + NaI + H_2O	Piston cylinder
BA-PC88	2	1400	60	STV301 + NaI	Piston cylinder - Fe-doped Pt capsule
BA-PC89	2	1400	60	STV301 + NaI	Piston cylinder - Fe-doped Pt capsule
BA-PC71	3.5	1600	60	STV301 + Xe + H_2O	Piston cylinder
BM-PC71	3.5	1600	60	MORB + Xe + H_2O	Piston cylinder
BA-PC73	3.5	1600	60	STV301+ NaI + Xe + H_2O	Piston cylinder
BM-PC73	3.5	1600	60	MORB + NaI + Xe + H_2O	Piston cylinder

689
690 Sample names: HPG stands for Haplogranite composition, BA for Basalt of Arc (IAB) composition, BM
691 for Basalt of MORB composition

Table 2: Major elements (EMPA), iodine and xenon (PIXE), and water (ERDA) compositions.

Starting materials and samples wt.%	SiO_2	TiO_2	Al_2O_3	FeO	MnO	MgO	CaO	Na_2O	K_2O	I Lα	I Lβ	Xe Lα	H_2O	Total
HPG (1)	73.65		11.77					4.66	4.26				5.02	99.36
IAB (2)	47.01	1.07	15.28	8.79	0.16	12.5	10.95	2.23	0.47					98.47
N-MORB (3)	49.97	2.27	13.68	12.69	0.22	6.83	10.56	2.69	0.27					99.54
HPGI-03	75.17		12.10					4.11	4.04	0.47	0.47		4.04	99.92
	(0.54)		(0.22)					(0.11)	(0.14)	(0.09)	(0.07)		(0.61)	
HPGI-05	74.43		11.91					4.10	3.93	0.46	0.45		5.48	100.3
	(0.55)		(0.31)					(0.18)	(0.19)	(0.06)	(0.07)		(0.82)	
HPGXe-02	71.33		11.99					4.61	4.13			4.00	5.06	
	(0.66)		(0.22)					(0.07)	(0.17)			(0.80)	(0.75)	100.8
HPGXe-C11	72.03		11.86					4.44	4.06			3.54	4.66	
	(0.67)		(0.27)					(0.12)	(0.12)			(0.50)	(0.70)	100.3
HPGXe-C17	69.91		11.67					4.23	3.95			1.89	7.75	
	(0.63)		(0.13)					(0.11)	(0.13)			(0.38)	(1.1)	99.36
HPGXe-C6	69.57		11.41					4.26	3.89			3.72	7.74	
	(0.44)		(0.20)					(0.13)	(0.24)			(0.53)	(1.02)	100.6
HPGXeI-04	71.48		11.75					4.35	3.81	1.33		3.64	4.37	
	(0.50)		(0.20)					(0.15)	(0.13)	(0.15)		(0.52)	(0.65)	100.7
BA - C7	45.72	1.12	14.91	8.51	0.17	11.85	10.65	2.60	0.32		0.48		3.97	100.3
	(0.43)	(0.04)	(0.18)	(0.30)	(0.05)	(0.12)	(0.16)	(0.08)	(0.04)		(0.07)		(0.60)	
BA-PC82	46.91	1.37	15.16	0.95	0.16	11.58	10.58	2.98	0.50		2.97		3.82	96.98
	(0.51)	(0.07)	(0.27)	(0.09)	(0.05)	(0.15)	(0.18)	(0.08)	(0.03)		(0.58)		(0.57)	
BA-PC83	47.86	1.47	15.63	1.20	0.15	11.79	10.82	2.87	0.49		2.67		1.64	96.59
	(0.45)	(0.09)	(0.28)	(0.07)	(0.07)	(0.15)	(0.22)	(0.08)	(0.04)		(0.58)		(0.25)	
BA-PC87	49.83	1.36	16.34	1.05	0.12	12.40	11.42	2.82	0.40		1.42		2.33	99.49
	(0.55)	(0.10)	(0.23)	(0.06)	(0.05)	(0.12)	(0.28)	(0.08)	(0.03)		(0.23)		(0.35)	
BA-PC88*,**	50.83	1.29	16.54	1.75	0.15	12.89	11.43	2.66	0.45		0.66		0.66	99.31
	(0.49)	(0.11)	(0.17)	(0.08)	(0.07)	(0.12)	(0.17)	(0.08)	(0.03)		(0.13)		(0.10)	
BA-PC89*	48.51	1.25	16.04	5.77	0.17	12.23	11.09	2.88	0.36		1.02		0.13	99.45
	(0.45)	(0.07)	(0.20)	(0.16)	(0.05)	(0.12)	(0.25)	(0.10)	(0.03)		(0.17)		(0.02)	
BA-PC71	51.41	1.20	16.91	0.29	0.15	13.34	12.07	2.48	0.57			0.27	1.26	
	(0.67)	(0.06)	(0.27)	(0.09)	(0.04)	(0.12)	(0.17)	(0.06)	(0.05)			(0.10)	(0.20)	99.96
BM-PC71	55.74	2.65	14.78	1.02	0.22	7.47	11.98	2.93	0.33			0.40 (0.21)	1.89	
	(0.67)	(0.07)	(0.28)	(0.26)	(0.04)	(0.13)	(0.23)	(0.10)	(0.05)				(0.28)	99.41
BA-PC73	50.04	1.41	16.35	0.15	0.09	12.32	11.65	2.79	0.48		1.81	0.19	1.48	
	(0.48)	(0.04)	(0.28)	(0.08)	(0.07)	(0.13)	(0.19)	(0.09)	(0.04)		(0.19)	(0.16)	(0.42)	98.75
BM-PC73	54.77	2.81	14.43	0.34	0.17	7.36	12.07	3.35	0.27		2.00	0.33	1.46	
	(0.35)	(0.06)	(0.19)	(0.10)	(0.06)	(0.08)	(0.12)	(0.12)	(0.05)		(0.21)	(0.19)	(0.41)	99.36

(1) Bureau and Keppler, 1999; (2) STV301, Pichant et al., 2002; (3) BN06-11, Prouteau and Scaillet 2013. * Fe-doped Pt capsules, **water leak during the run. Sample names: HPG stands for Haplogranite composition, BA for Basalt of Arc (IAB) composition, BM for Basalt of MORB composition

Table 3: Concentrations and partition coefficients calculated from data collected in situ at pressures and temperatures

Exp.	Starting glass	T°C	P GPa	Xe_{fluid} wt.%	$Xe_{melt\ or\ glass}$ wt.%	$D^{Xe}_{f/m}$	I_{fluid} wt.%	$I_{melt\ or\ glass}$ wt.%	$D^{I}_{f/m}$
#01	HPGXe-C11	761	1.44	3.78	0.0148	255			
		692	1.31	3.88	0.0111	348			
		684	1.21	3.93	0.0014	2748			
		RT	RP	4.33					
		RT**	RP**		0.0283*			< DL	
		RT**	RP**		0.0345*			< DL	
#02	HPGXe-C11	>851 [S]	>1.68	2.915					
		851 [CS]	1.68	3.74	0.5645	0.15			
		791	1.50	5.16	0.1778	6.63			
		741	1.40	4.74	0.0252	188			
		692	1.31	4.011	0.0191	210			
		RT	RP	4.97					
		RT**	RP**		< DL				
		RT**	RP**		< DL				
#03	HPGXeI-04	794	1.51	4.6	0.053	86.4	1.72	1.77	0.97
		789	1.50		0.039			1.256	
		RT**	RP**		0.9682*			0.2547*	
		RT**	RP**		0.9953*			0.3153*	

Exp. Experiment. [S]supercritical fluid, in agreement with complete miscibility data for HPG-water after Bureau and Keppler (1999); [CS] close to supercritic *quench bubbles included, **from PIXE; Analytical uncertainties are 10% for SXRF, 5% for PIXE analysis. DL detection limit.
Uncertainty on pressure is 0.2 GPa. Temperatures are corrected from the calibration performed at room pressure from chemicals of known melting points.

Figures Captions

Figure 1: PIXE spectrum for A-HPGI-03 sample, B-BA-PC82 sample. x-rays are labelled. The dark line represents the experimental spectrum, dotted and dashed lines correspond to the theoretical fits for potassium K, calcium Ca and iodine I x-rays (see legends).

Figure 2: Xe wt.% **(A)** and I wt.% **(B)** concentrations measured in haplogranite (HPG) and basaltic glasses versus Pressure (GPa). These concentrations reflect the solubility data, except for I at 3.5 GPa, because the total amount of I in the starting compositions corresponds to the concentrations measured after the experiment. The concentration for Xe are in good agreement with the solubility measured in tholeiites (Schmidt and Keppler, 2002). Dark squares: HPG enriched in Xe, open squares: HPG enriched in both Xe and I, open circles: basalts enriched in Xe, dark circle: Basalts enriched in both Xe and I, diamonds: data from Schmidt and Keppler (2002). **(C)** Halogen element (I, Br, Cl) solubility in wt.% versus pressure in GPa for HPG melt and I solubility in IAB melts for comparison at low pressures (P max 0.4 GPa). Data for I (HPG: dark squares, IAB: open square) are from this study, data for Br (HPG: dark triangle) are from Bureau and Métrich (2003), data for Cl (HPG black circles) are from Webster (1997). Uncertainties are within de size of the symbols. All halogens exhibit similar ranges of solubility values in both melt compositions.

Figure 3: SEM images of the three quenched samples recovered from HP-HT DAC experiments. A. Sample chamber of exp #01, the arrow indicates the area zoomed in fig. 5.B ; B. Zoom on the large glassy globules showing the high density of Xe-I-rich bubbles that contaminate the glass analysis; C High density of Xe-I-rich bubbles in the glass that strongly contaminate the analysis. D. exp #02, small glassy globule, without bubbles.

Figure 4: In situ SRXF spectra of Xe content in DAC, in supercritical fluid (green) at T>851°C, aqueous fluid (red) and silicate melt (black) at 1.68 GPa and 851°C for experiment #02. The Kα and Kβ rays of Xe are observed at 29.78 keV and 33.62 keV respectively, measurements are performed in the supercritical fluid, then in the aqueous fluid and silicate melt at equilibrium at 860°C and 1 GPa. Xe is immediately lost from the silicate melt to the aqueous fluid formed upon cooling the supercritical fluid.

Figure 5: Pressure versus partition coefficient, $D^{f/m}$, for HPG starting glasses enriched in I and Xe. I data: this study in the presence of Xe (grey square), from Bureau et al., 2016 (open squares); Xe

data: this study (dark circles grey circle in the presence of I). The cross represents the uncertainties. The inset represents all the data, including high $D_{f/m}$. The diagram shows a stronger affinity of Xe for the fluid phase compared to I with respect to pressure (i.e. magma ascent), except at high P where the opposite is observed, and the consequent decoupling of both elements. Grey symbols represent partition coefficient of I (square) and Xe (circle) when both elements are present in the system. They show that the presence of Xe has no influence on I partitioning and reciprocally. The slope change in the pressure evolution in $D_I^{f/m}$ at 0.5 GPa, might relate to a change of retention mechanism of iodine in the silicate melt (see text).

Figure 6: Pressure versus temperature conditions of the three series of partitioning experiments (Table 3): #01 (open squares), #02 (open triangles), #03 (open circles Xe and I present), performed with starting glasses HPGXe-C11, HPGXeI-04 (see Table 1). Labels are the partition coefficients measured for Xe ($D_{Xe}^{f/m}$). The grey curve is the melting curve of Xe after Belonoshko et al. (2006). The dashed curve is the P-T regime of crustal xenoliths after Rodriguez-Vargas et al. (2005). The P-T regime of the oceanic slab is out of the scale of the diagram. Results show a good agreement between the *P* and *T* conditions of one experiment performed 10°C below total miscibility (02, 851°C, 1.68 GPa) where most of the Xe is still in the silicate melt ($D_{Xe}^{f/m}$=0.15). All the other experiments are located below the Xe melting curve, when most of the Xe, if not all, is transferred to the fluid phase. It suggests that Xe is recycled in the mantle in aqueous fluids where it can be incorporated in silicate melts.

Figure 7: In situ Raman spectroscopy in the DAC in the supercritical fluid (860°C, 1.6 GPa), and in the aqueous fluid and silicate melt (850°C, 1.5 GPa). This experiment was performed with a I-free HPG glass and I-enriched aqueous fluid (H_2O-NaI 20 g/l) as starting materials following the protocol defined in Bureau et al. (2016). We observe a band at around 134 cm^{-1} corresponding to I-I bond stretching vibrations (Deplano et al., 1999).

Figure 1

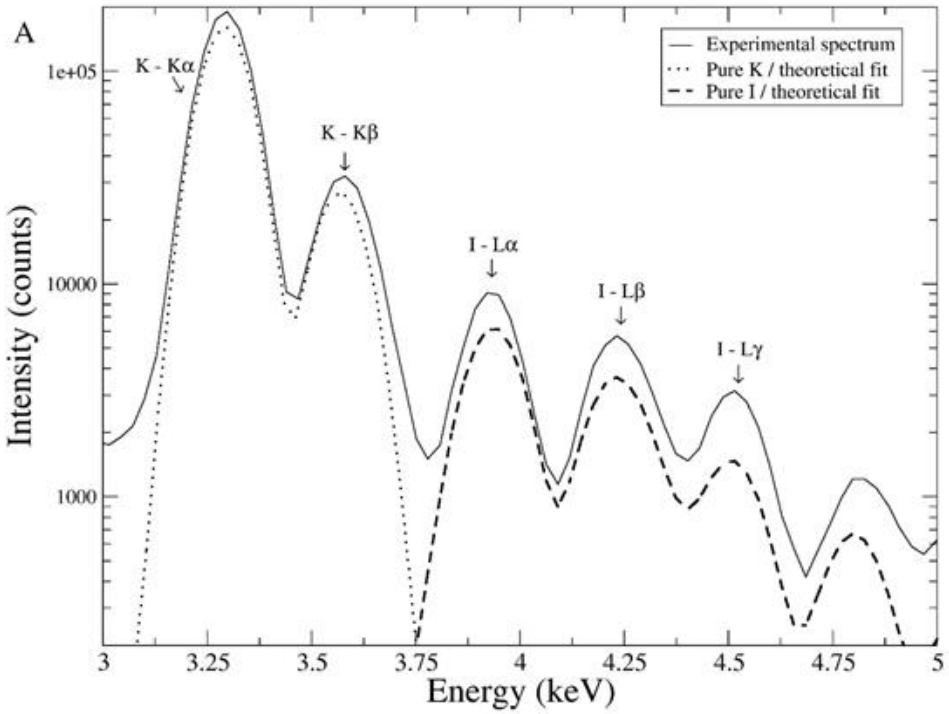
A
Experimental spectrum
Pure K / theoretical fit
Pure I / theoretical fit
K - Kα
K - Kβ
I - Lα
I - Lβ
I - Lγ
Intensity (counts)
1e+05
10000
1000
3
3.25
3.5
3.75
4
4.25
4.5
4.75
5
Energy (keV)

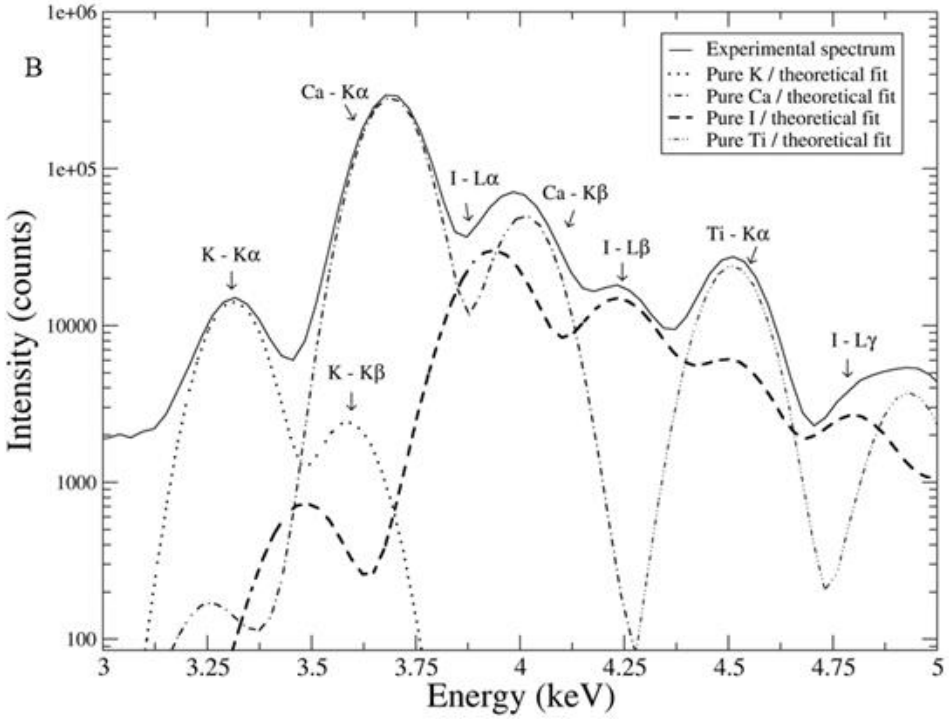
B
Experimental spectrum
Pure K / theoretical fit
Pure Ca / theoretical fit
Pure I / theoretical fit
Pure Ti / theoretical fit
Ca - Kα
I - Lα
Ca - Kβ
I - Lβ
Ti - Kα
K - Kα
K - Kβ
I - Lγ
Intensity (counts)
1e+06
1e+05
10000
1000
100
3
3.25
3.5
3.75
4
4.25
4.5
4.75
5
Energy (keV)

Figure 2

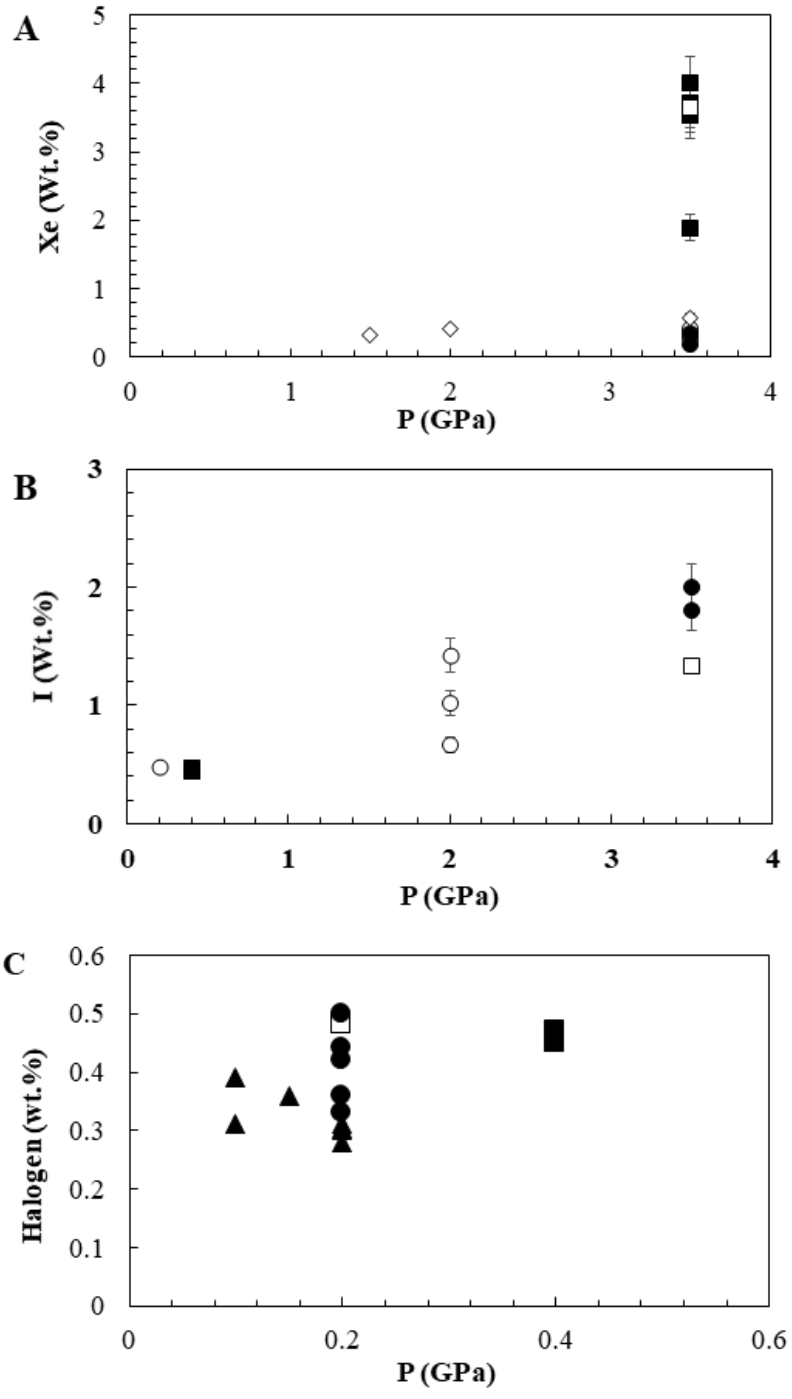

Figure 3

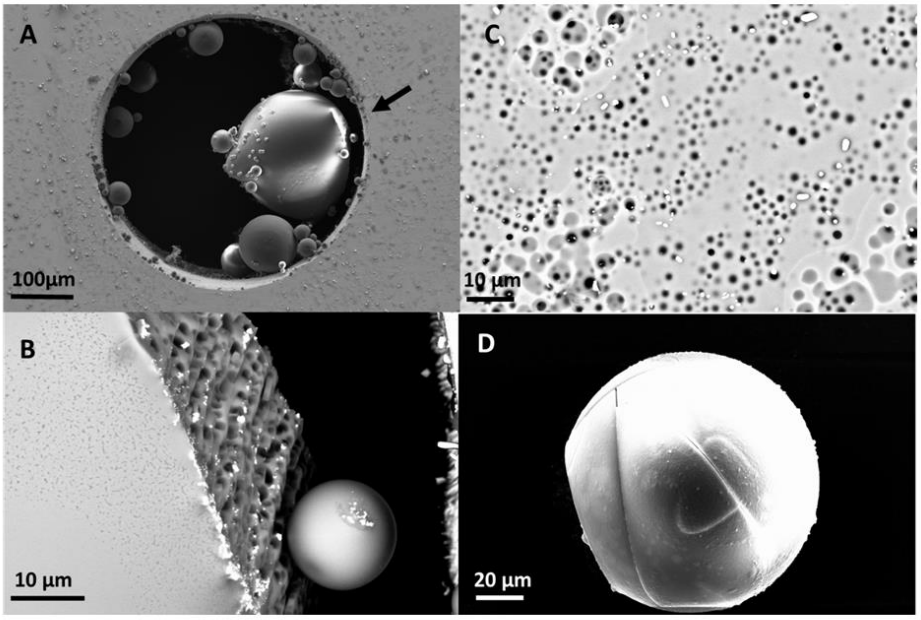

Figure 4

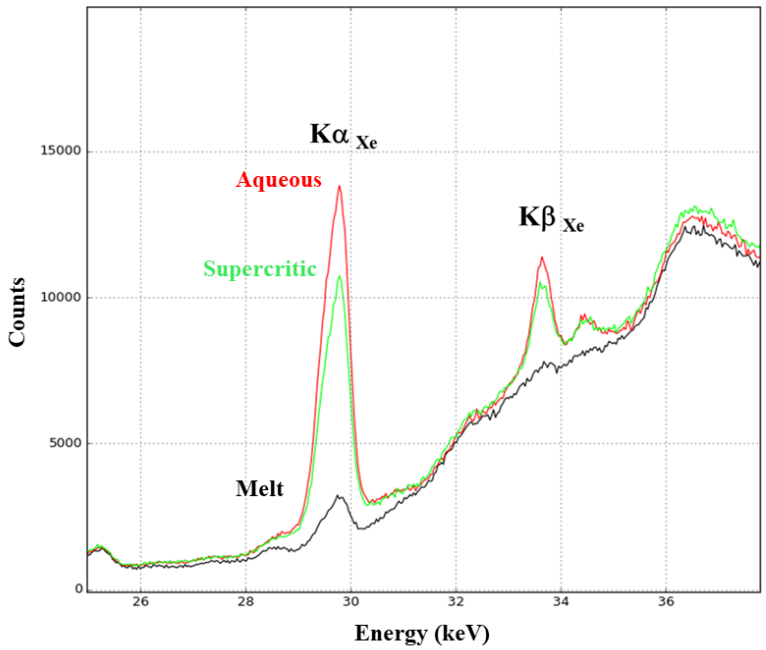

Figure 5

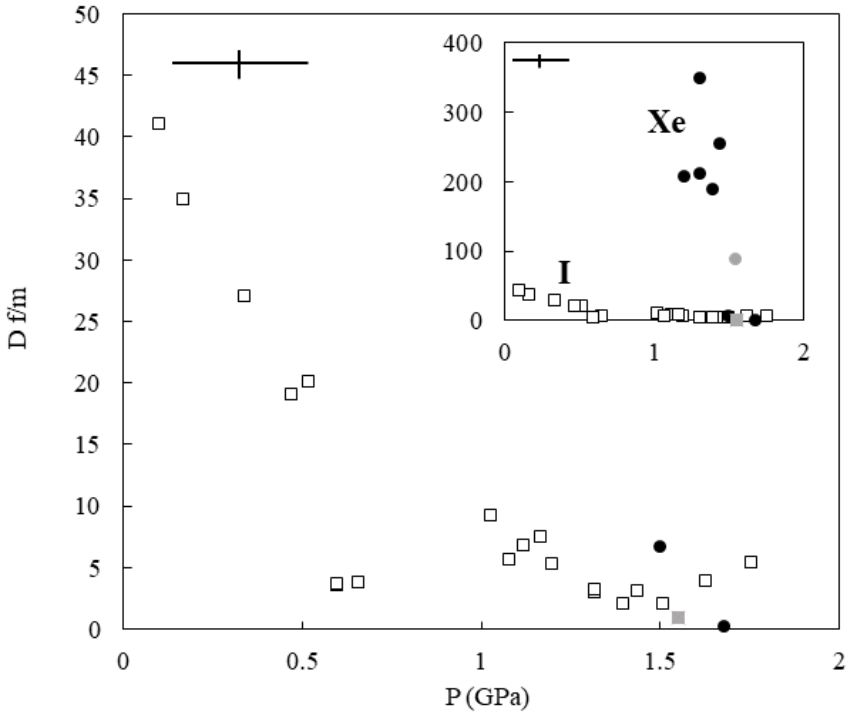

Figure 6

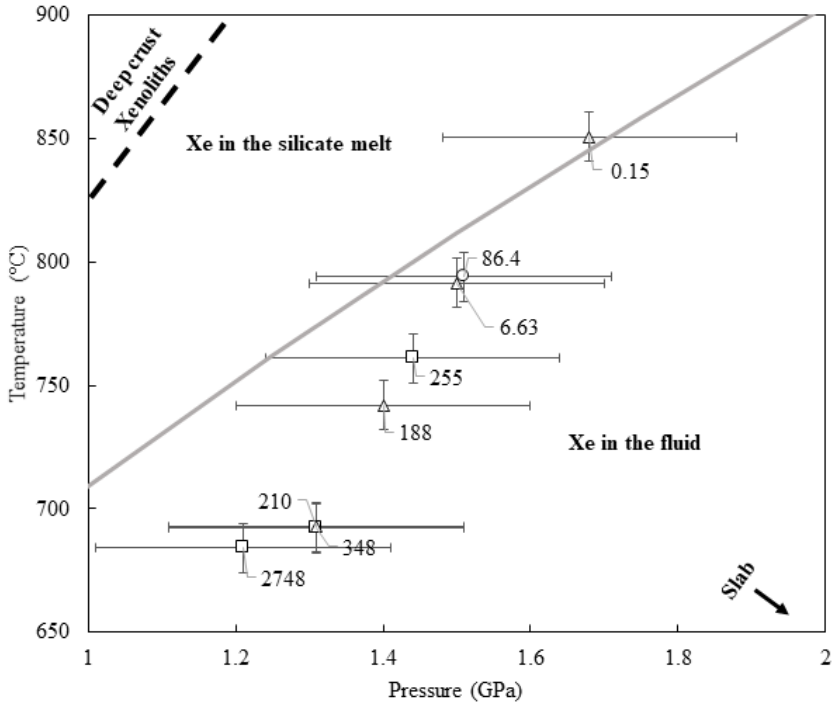
Deep crust
Xenoliths
Xe in the silicate melt
Xe in the fluid
0.15
86.4
6.63
255
188
210
348
2748
Slab
Temperature (°C)
Pressure (GPa)
900
850
800
750
700
650
1
1.2
1.4
1.6
1.8
2

Figure 7

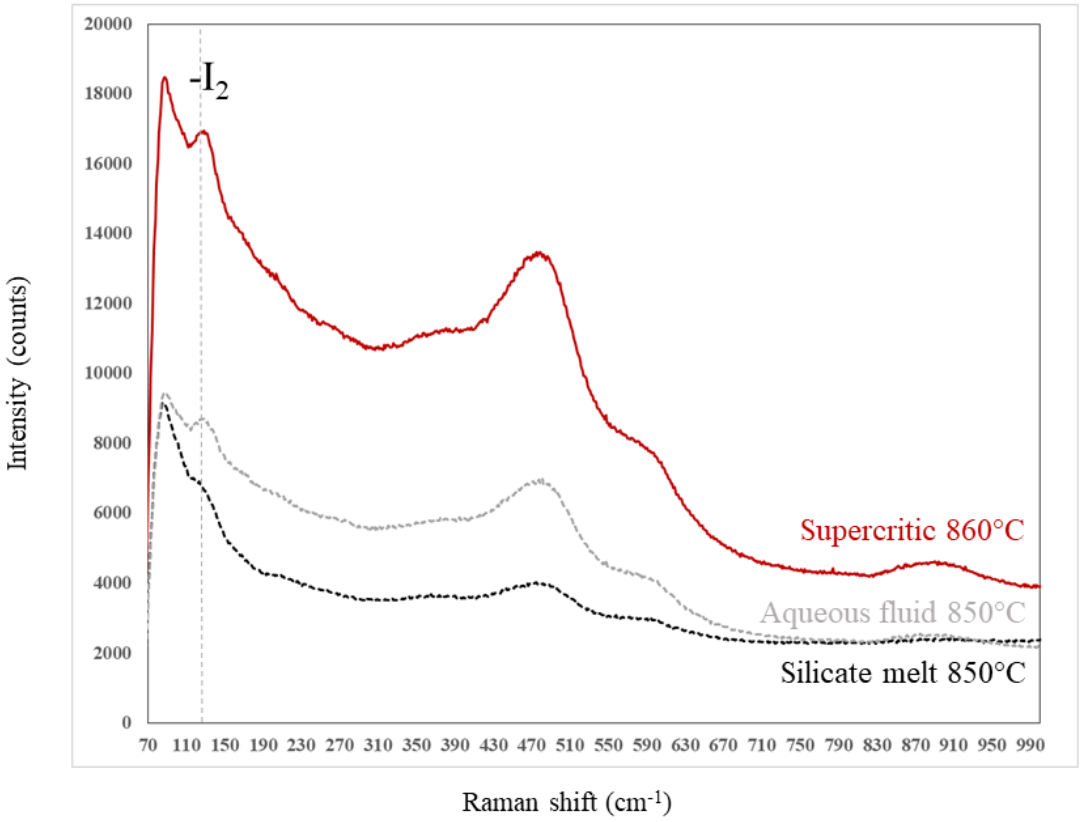
-I2
Supercritic 860°C
Aqueous fluid 850°C
Silicate melt 850°C
Intensity (counts)
Raman shift (cm-1)
20000
18000
16000
14000
12000
10000
8000
6000
4000
2000
0
70 110 150 190 230 270 310 350 390 430 470 510 550 590 630 670 710 750 790 830 870 910 950 990